Chinese Physics Letters

LETTER

Switchable Magnonic Topology with Transport Fingerprints in Two-Dimensional Ferromagnet $CrVI_6$

Cite as: Yingxi Bai *et al*. 2026 *Chin. Phys. Lett.* **43** 060712

Recommended Articles

Topological Chiral Magnons in the Altermagnet AgF_2 Monolayer
J. W. González, R. A. Gallardo, N. Vidal-Silva, and A. M. León
Chin. Phys. Lett. **43**, 020705 (2026)

Magnon Splitting and Magnon Spin Transport in Altermagnets
Kun Wu, Jianting Dong, Meng Zhu, Fanxing Zheng, and Jia Zhang
Chin. Phys. Lett. **42**, 070702 (2025)

Higher-Order Topological States in Chiral Split Magnons of Honeycomb Altermagnets
Xuan Guo, Meng-Han Zhang, and Dao-Xin Yao
Chin. Phys. Lett. **42**, 120703 (2025)

Giant Uncompensated Magnon Spin Currents in X-Type Magnets
Zi-An Wang, Bo Li, Shui-Sen Zhang, Wen-Jian Lu, Mingliang Tian, Yu-Ping Sun, Evgeny Y. Tsymbal, Kaiyou Wang, Haifeng Du, and Ding-Fu Shao
Chin. Phys. Lett. **42**, 110713 (2025)

Two-Dimensional XY Ferromagnet Induced by Long-Range Interaction
Tianning Xiao, Dingyun Yao, Chao Zhang, Zhijie Fan, and Youjin Deng
Chin. Phys. Lett. **42**, 070002 (2025)

Topological Degeneracy Induced Flat Bands in Two-Dimensional Holed Systems
Yuge Chen, Hui Yu, Yun-Peng Huang, Zhen-Yu Zheng, and Jiangping Hu
Chin. Phys. Lett. **42**, 090714 (2025)

A series journal of Chinese Physical Society distributed by IOP Publishing

Chinese Physics Letters

Chin. Phys. Lett. **43** 060712 (2026)

LETTER

DOI: 10.1088/0256-307X/43/6/060712
CSTR: 32039.14.0256-307X.43.6.060712

Switchable Magnonic Topology with Transport Fingerprints in Two-Dimensional Ferromagnet $CrVI_6$

Yingxi Bai(白英希), Xiaoran Feng(冯晓冉), Bo Yuan(袁博), Zhiqi Chen(陈之祺), Ying Dai(戴瑛)*, Baibiao Huang(黄柏标), and Chengwang Niu(牛成旺)*

School of Physics, State Key Laboratory of Crystal Materials, Shandong University, Jinan 250100, China

*Corresponding authors. Email: daiy60@sdu.edu.cn; c.niu@sdu.edu.cn

Topological magnons offer a charge-free platform for low-dissipation spintronic devices. However, studies on magnonic topological phase transitions (TPTs) in experimentally synthesized materials remain limited. Here, we introduce a general mechanism for achieving controllable TPTs in topological magnonics. Remarkably, successive TPTs among the normal magnon insulator (NMI), topological magnon insulator (TMI), and second-order topological magnon insulator (SOTMI) phases are realized, with distinct topological fingerprints identifying each phase, i.e., integer Chern number C and chiral edge states for TMI, whereas nonzero fractional corner charge $Q^{(3)}$ and corner states for SOTMI. Combined with first-principles calculations, we demonstrate the experimentally synthesized 2D ferromagnet $CrVI_6$ as an ideal material realization of the proposed successive TPTs. Moreover, we find that the switchable TPTs in $CrVI_6$ monolayer are accompanied by pronounced and distinct changes in thermal, spin, and valley transport responses, including the magnon Hall effect, magnon Nernst effect, and their valley counterparts of magnon valley Hall effect and magnon valley Nernst effect. These transport responses not only reveal the previously overlooked TPTs, but also offer experimentally accessible means to distinguish the different magnonic topological phases.

Magnons, as the quantized collective excita tions of spin waves, have emerged as promising carriers of spin and heat due to their charge neutrality and inherently low dissipation [1−11]. Remarkably, the discovery of magnon Hall effect (MHE) in $Lu_2V_2O_7$ inspires the extension of topological band theory to bosonic quasiparticles [12]. The field is now advancing at an impressive pace, with the proposal and verification of diverse magnonic topological phases, including topological magnon insulators (TMIs), Dirac/Weyl magnons, and second-order topological magnon insulators (SOTMIs) [13−25]. On the experimental front, topological magnons have been successfully confirmed in materials such as CrI_3, $CrSiTe_3$, and Mn_5Ge_3 [26−28], while inelastic neutron scattering have enabled direct mapping of nontrivial magnon band structures. Moreover, thermal Hall measurements in magnets have revealed clear signatures of topological magnon transport [29,30]. These advances not only deepen our understanding of magnonic topology but also open new avenues for low-power spintronic applications and quantum information technologies.

Topological phase transitions (TPTs) serve as powerful tools for tuning quantum states of matter, enabling dynamic control over transport, symmetry, and topology [31−41], and it would be of great significance to realize TPT in a experimentally feasible candidate. For instance, a TPT driven by the thickness of HgTe in HgTe/CdTe quantum well leads to the emergence of quantum spin Hall states [42], while in photonic systems, $Ge_2Sb_2Te_5$-based material phase transitions have been employed to reversibly control topological phases in photonic topological insulators [43]. In magnonic systems, the fine-tuning of topologically nontrivial states holds great promise for engineering spin transport without involving charge currents, which is highly desirable for next-generation low-dissipation spintronic applications [44]. A viable platform must not only host external modulated magnonic TPTs, but also exhibit well-separated and detectable magnonic transport responses that signal different topological phases. To date, however, no experimentally accessible material system has simultaneously fulfilled these dual demands, resulting in a significant barrier to realizing functional and tunable topological magnonic platforms.

In this Letter, employing the honeycomb lattice, we demonstrate the emergence of long-awaited TPTs among the normal magnon insulator (NMI), TMI, and SOTMI phases in valley-polarized magnons. For which, a noncentrosymmetric Heisenberg-Dzyaloshinskii-Moriya (DM) model, in contrast to previously reported ones, with two inequivalent magnetic sublattices is constructed. Remarkably, we identify the experimentally synthesized two-dimensional ferromagnet $CrVI_6$ monolayer as a realistic material platform that naturally realizes the proposed TPTs. Its noncentrosymmetric lattice with inequivalent magnetic ions generates the pronounced intrinsic valley polarization. Moreover, the strain-engineered TPTs among SOTMI, TMI, and NMI phases in $CrVI_6$ monolayer are accompanied by distinct signatures in both total and valley-dependent magnonic transport properties. These transport signatures form a clear basis for the unambiguous experimental discrimination of these topological phases. Our results not only enrich prominent physical phenomena of topological magnons, but also pave the way for future exploration and device-level implementation of reconfigurable magnonic topological states.

Rationale and Model. To elucidate the key mechanisms of successive magnonic TPTs and establish general design principles for tunable topology magnons, we begin our discussion with the insightful noncentrosymmetric Heisenberg-DM model

$$H = \sum_{(i,j)\in\mathcal{N}} J_{ij}\cdot(\boldsymbol{S}_i\cdot\boldsymbol{S}_j) + \sum_{(i,j)\in\mathcal{N}} \boldsymbol{D_{ij}}\cdot(\boldsymbol{S}_i\times\boldsymbol{S}_j) + A_z\sum_i (S_i^z)^2, \quad (1)$$

where $\mathcal{N}$ includes both the nearest-neighbor (NN) and next-nearest-neighbor (NNN) interactions. J_{ij} denotes the Heisenberg exchange parameter between spins $\boldsymbol{S}_{i/j}$, and $\boldsymbol{D_{ij}}$ represents the corresponding Dzyaloshinskii-Moriya interactions (DMIs), expressed as $\boldsymbol{D_{ij}} = D_{ij}\hat{z}$. A_z is the single-ion anisotropy along the z-axis. The spin operator is defined as $\boldsymbol{S}_i = (S_i^x, S_i^y, S_i^z)$. To facilitate further analysis, we apply the Holstein-Primakoff and Bogoliubov transformations to map the spin operators onto bosonic operators and diagonalize the Hamiltonian [45,46]. For the noncentrosymmetric honeycomb lattice depicted in

Received 30 December 2025; accepted 29 April 2026; published 11 June 2026

© 2026 Chinese Physical Society and IOP Publishing Ltd. All rights, including for text and data mining, AI training, and similar technologies, are reserved.

Check for updates

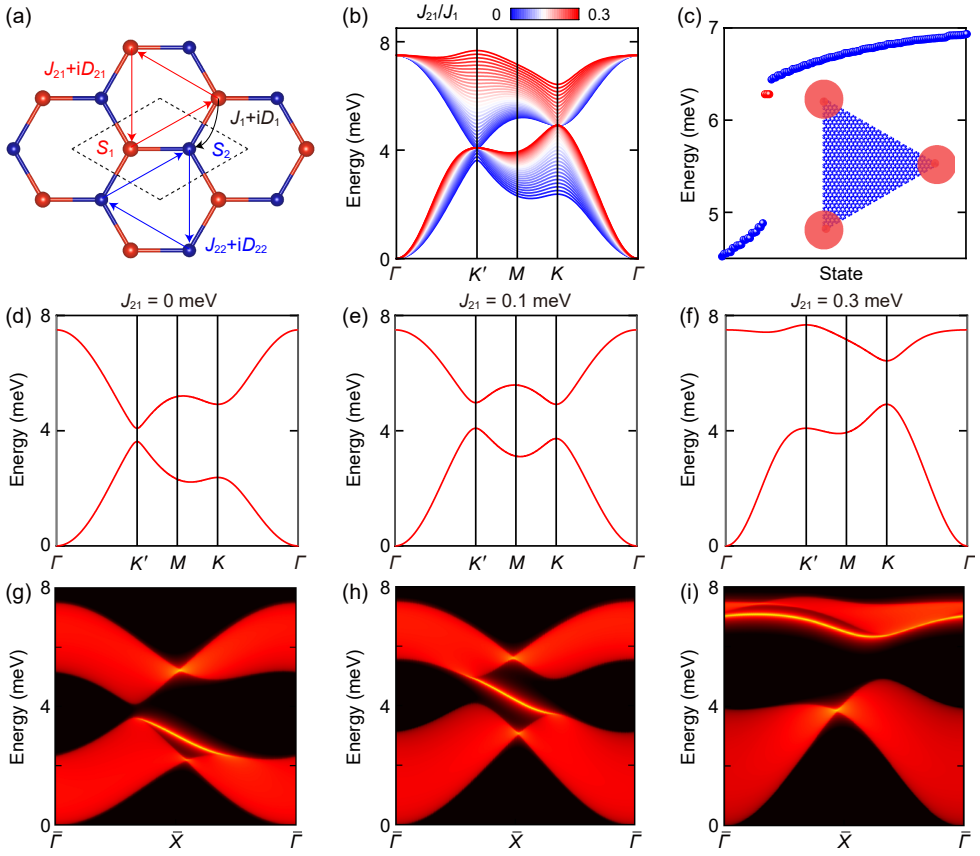

Fig. 1. (a) Schematic illustration of the Heisenberg-DM model on a two-dimensional noncentrosymmetric honeycomb lattice. (b) Magnonic band strucures of the Heisenberg-DM model under varying parameters J_{21}/J_1, with fixed parameters $J_1 = 1$ meV, $D_{21} = -D_{22} = -0.08\ J_1$, and $J_{22} = 0$ meV. (c) Energy spectrum of the triangular nanoflakes based on the Heisenberg-DM model, corresponding to the floating edge state in (i). Bulk states (blue dots) and topologically nontrivial corner states (red dots) are explicitly marked. (d)–(f) Magnonic band strucures and (g)–(i) edge states for the Heisenberg-DM model with increasing NNN Heisenberg interaction J_{21}, under fixed parameters $D_{21} = -D_{22} = -0.08\ J_1$ and $J_{22} = 0$ meV. The chiral state in (h) confirming the topological nature characterized by a Chern number $C = 1$.

Fig. 1(a), the asymmetry in different spin magnitudes $\boldsymbol{S}$ naturally divides the NNN parameters J_2 and D_2 into two categories, corresponding to the $\boldsymbol{S}_1$ and $\boldsymbol{S}_2$ sublattices, respectively. Here, J_2 and D_2 denote the NNN Heisenberg exchange interactions and NNN DMIs along the z-axis.

Without loss of generality, we fix the exchange parameters as $D_1 = J_{22} = 0$ and $D_{22} = -D_{21} = D_2$ in order to simplify the analysis, and all the parameters are scaled with the NN Heisenberg exchange parameter J_1. Firstly, focusing on the impact of NNN Heisenberg exchange parameter J_{21}, we present in Fig. 1(b) the evolution of magnonic bands versus J_{21}, with D_2 constrained to $0.08J_1$. As expected, the band gaps can be effectively engineered by J_{21}. Neglecting J_{21}, the above model hosts a NMI phase, as indicated by the gapped band structure in Fig. 1(d) and the absence of gapless edge state in Fig. 1(g). Two magnonic bands approach each other as the J_{21} is increased, and, moreover, a band gap closing and reopening process emerges at the K' point across the critical point $J_{21} = 0.03J_1$. Remarkably, the magnonic band gap closes once more, though at the K point instead, specifically for $J_{21} = 0.19J_1$. Figure S1 of Supplementary Materials (SM) shows the magnonic edge states at the gap-closing and reopening points ($J_{21}/J_1 = 0.03$ and 0.19, with $D_2/J_1 = 0.08$), which clearly illustrates the topological phase boundaries of the Heisenberg-DM model (see the SM). In fact, TPTs are typically signaled by the band gap closure and reopening. Therefore, the sequential occurrence of both events in our Heisenberg-DM model indicates a rich topological phase diagram with two distinct TPTs.

Taking $J_{21} = 0.1J_1$ and $J_{21} = 0.3J_1$ as the examples, we then elucidate the topologically nontrivial characters and the topological phase transitions. Figures 1(e) and 1(f) present their magnonic band strucures, where the insulating gaps are clearly visible. For $J_{21} = 0.1J_1$ case, the TMI phase of the gap can be explicitly confirmed via calculations of the magnonic Wannier center (MWC), which results in $C = 1$ (see the SM), and the emergence of one chiral edge state in the nanoribbon as illustrated in Fig. 1(h). However, for the case of $J_{21} = 0.3J_1$, one floating edge state emerges within the magnonic band gap, as shown in Fig. 1(i), which is generally considered as a key signature of the second-order topological phase. To quantitatively identify the nontrivial topology, we evaluate the topological index $\chi^{(3)}$ and fractional corner charge $Q^{(3)}$, defined as

$$\chi^{(3)} = ([K_1^{(3)}], [K_2^{(3)}]);\ Q^{(3)} = 1/3[K_2^{(3)}] \bmod 1. \tag{2}$$

Here $[K_p^{(n)}] = \#K_p^{(n)} - \#\Gamma_p^{(n)}$ denote the difference in the number of magnon bands involved in the topological characterization that carry the C_n rotational eigenvalues $\Pi_p^{(n)}$ at the K and Γ points [47]. The computed topological indices and fractional corner charge are $\chi^{(3)} = (-1, 1)$ and $Q^{(3)} = 1/3$, respectively, providing definitive evidence of the SOTMI phase. Additionally, figure 1(c) presents the energy spectrum of a triangular nanoflake and the distribution of wave functions for these states. Three degenerate states (red dots) can be clearly observed in the magnonic gap, and their wave functions are well localized at the three corners of the triangular nanoflake.

Another critical factor governing the magnonic TPTs is the NNN DMI. To map out a more comprehensive understanding of the topological magnons, we provide a phase diagram with respect to the J_{21} and D_2. Clearly, figure 2(a) indicates that there are three distinct magnonic states, i.e., NMI, TMI, and SOTMI, separated by two dashed lines representing the topological phase boundaries. When $D_2 = 0$, the preservation of pseudo-spin time-reversal symmetry $\mathcal{T}$

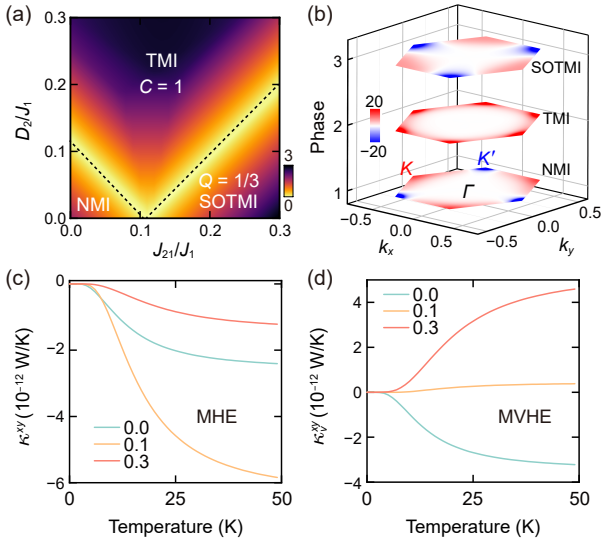

Fig. 2. (a) Phase diagram for the Heisenberg-DM model as functions of J_{21}/J_1 and D_2/J_1 with $\boldsymbol{S}_1 = 3\boldsymbol{S}_2/2 = 3/2$ and $J_{22} = 0$. The color bar represents the width of the band gap. (b) K-space distributions of Berry curvatures for the Heisenberg-DM model with different topological phases, corresponding to TPTs in (a). Temperature dependence of (c) thermal Hall conductivity and (d) valley thermal Hall conductivity of the Heisenberg-DM model as functions of J_{21}/J_1, revealing transport properties are strongly coupled to the magnonic topological phases of the Heisenberg-DM model.

enforces valley degeneracy between the K and K' points, restricting TPT to a single pathway between the NMI and SOTMI. Moreover, taking D_2 into account, breaking $\mathcal{T}$-symmetry via NNN DMI spontaneously polarizes the magnonic valleys. As a direct consequence, the valley-asymmetric bands and distinct energy gaps emerge, leading to the feasibility of magnonic TPTs among NMI, TMI, and SOTMI phases.

Remarkably, as is well known, the Berry curvatures originate from the geometric properties of energy bands, with the distribution of Berry curvatures reshaping in momentum space accompanied with the TPTs [48,49]. Figure 2(b) presents the k-space distributions of Berry curvatures with three representative values of $J_{21} = 0$, $J_{21} = 0.1J_1$, and $J_{21} = 0.3J_1$, which corresponde to NMI, TMI, and SOTMI phases, respectively. When the TPT from NMI to TMI occurs, the sign of Berry curvatures flips at the K' valley, and moreover the same positive sign at both K and K' for TMI suggests a nonzero integral of the Berry curvatures where an integer Chern number of $C = 1$ is indeed obtained. When the flips of sign for Berry curvatures occurs at K as well, another TPT is taking place as the system changes its character from a TMI to a SOTMI.

More importantly, both the MHE and magnon valley Hall effect (MVHE) are directly related to the Berry curvatures [50,51], as the thermal Hall conductivity κ^{xy} and valley thermal Hall conductivity κ_v^{xy} are respectively given by

$$\begin{aligned}\kappa^{xy} &= -\frac{k_B^2 T}{(2\pi)^2\hbar}\sum_n \int_{BZ} c_2(n_B(\varepsilon))\Omega_n^{xy}(k)\mathrm{d}k,\\ \kappa_v^{xy} &= -\frac{k_B^2 T}{(2\pi)^2\hbar}\sum_{n,k} c_2(n_B(\varepsilon))[\Omega_{n_K}^{xy}(k) - \Omega_{n_{K'}}^{xy}(k)],\end{aligned} \tag{3}$$

where $n_B(\varepsilon)$ denotes the Bose distribution function with $n_B(\varepsilon) = [\exp(\frac{\varepsilon-\mu}{k_B T}) - 1]^{-1}$, and $c_2(x) = (1+x)\ln^2[(1+x)/x] - \ln^2 x - 2Li_2(-x)$. μ is the chemical potential and Li_2 indicates the polylogarithm function. As shown in Fig. 2(c), steming from the Berry curvature near the K and K' valley, the giant MHE emerges in the TMI phase. However, the valley-resolved contributions vanish in the TMI phase due to the identical polarity of Berry curvature at the K and K' valleys, thereby suppressing the experimental signature of the MVHE, as illustrated in Fig. 2(d). Interestingly, the giant MVHE is obtained in both the NMI and SOTMI phases. And moreover the magnonic TPTs invert the valley-contrasted Berry curvatures, inducing sign reversal of valley thermal Hall conductivity between the NMI and SOTMI phases. Thus, clear experimental signatures are obtained to distinguish all three topological phases. These results reveal a strong interplay among magnonic band topology, valley degrees of freedom, and thermal/spin transport phenomena, opening up new possibilities for detecting and manipulating topological magnons.

Material Realization. Building on the above model analysis, we then demonstrate that the experimentally feasible $CrVI_6$ monolayer, which has been successfully fabricated through mechanical exfoliation [52], is a promising candidate material exhibiting tunable magnonic topological phases, valley physics, and transport properties. As illustrated in Fig. 3(a), $CrVI_6$ monolayer is a 2D ferromagnet with a noncentrosymmetric honeycomb lattice, belonging to the magnetic space group $P312'$ (No. 149.23). The optimized lattice constant of the $CrVI_6$ monolayer is $a = 7.034$ Å. The magnetic exchange parameters of the $CrVI_6$ monolayer are obtained through the Green's function method based on magnetic force theory (MFT) [53], which are in good agreement with those obtained via the energy-mapping methods [54]. According to the Moriya's rules, the DM vector aligns with the Cr-V bond, leading to $D_1^z = 0$ [55]. With perpendicular magnetic anisotropy, we exclusively consider the z-component of DMI, which is the critical mediator of magnonic topological properties.

Figure 3(b) presents the magnonic band structure of the $CrVI_6$ monolayer. Clearly, a pronounced valley polarization with a magnitude of $\Delta K = 0.83$ meV emerges at the K and K' points. This is due to the absence of both inversion symmetry $\mathcal{P}$ and pseudo-spin time-reversal symmetry $\mathcal{T}$. As detailed in Table SI of the SM, the NNN Heisenberg interactions J_{21} and D_{21} for Cr atoms in $CrVI_6$ monolayer are comparable to the CrI_3 monolayer (see the SM) [26,56]. However, the weak magnetic moments of V result in the small NN Heisenberg interaction J_1, and, moreover, the relatively weak Heisenberg exchange interactions and the different spin vectors $\boldsymbol{S}$ between two magnetic atoms Cr and V lead to a low magnon excitation energy and a wide magnonic energy gap, making the $CrVI_6$ monolayer is favorable for experimental detection.

To confirm the topologically nontrivial nature of the obtained magnonic insulating gap, we then calculate the C_3 rotational eigenvalues $\Pi_p^{(3)}$ of the $CrVI_6$ monolayer. As expected, the topological indices and fractional corner charge indeed acquire nonzero values of $\chi^{(3)} = (-1, 1)$ and $Q^{(3)} = 1/3$, respectively, confirming the SOTMI nature in $CrVI_6$ monolayer. Moreover, one of the key features of SOTMI is the existence of exotic corner states in the insulating bulk energy gap. To illustrate this, a triangular nanoflake with C_3 rotational symmetry is constructed and the energy spectrum is presented in Fig. 3(c). Obviously, one observes three states (red dots) with their spatial distribution well localized at the three corners of the nanoflake, in direct agreement with the nonzero $\chi^{(3)}$ and $Q^{(3)}$.

Following this initial analysis, we investigate the magnonic TPTs in $CrVI_6$ monolayer under strain engineering, where strain effects are captured by exchange interactions calculated at strain-dependent lattice constants in the Heisenberg Hamiltonian (see the SM). Similar to the model analysis, the magnonic energy gaps and band topology are highly sensitive to the ratio J_{21}/J_1. As illustrated in Fig. 3(d), the Heisenberg exchange parameter J_1 increases while the parameter J_{21} decreases, i.e., the ratio J_{21}/J_1 decreases, with the lattice parameters increasing. And the band gap closing and reopening occurs respectively at the K and K' points under critical strains of 1.8% and 4.6%, revealing the magnonic TPTs associated with the decreasing J_{21}/J_1. When the lattice parameter lies between the two critical values, the TMI phase is obtained. For example, as illustrated in Figs. 3(e) and 3(f) with a 3% tensile strain, the Chern number indeed acquires an integer value of $C = 1$, and the emergence of one chiral edge state is clearly visible. With further increasing strain, all of considered topological invariants become zero, and the system becomes a NMI. All in all, a cascade of TPTs driven by the critical exchange ratio J_{21}/J_1

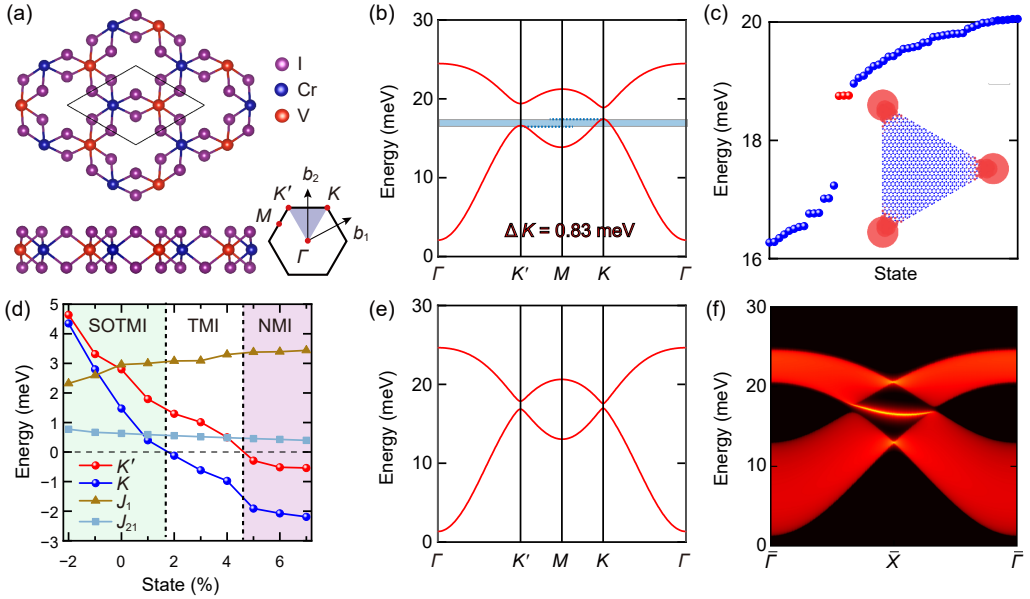

Fig. 3. (a) Top and side views of the $CrVI_6$ monolayer with the hexagonal first Brillouin zone. (b) Magnonic band structure of the $CrVI_6$ monolayer. (c) Energy spectrum of triangular nanoflakes of the $CrVI_6$ monolayer, highlighting bulk states (blue dots) and topologically nontrivial corner states (red dots). (d) Magnon gap at K and K' points and Heisenberg interaction parameters of the $CrVI_6$ monolayer as functions of strain with corresponding topological indices. (e) Magnonic band structure and (f) edge states of the $CrVI_6$ monolayer under 3% tensile strain, indicating the emergence of chiral edge states.

provides definitive evidence of strain-tunable magnon topology in the $CrVI_6$ monolayer, in full agreement with the Heisenberg-DM model discussed above.

Magnon Transport with Topological Switch. TPTs fundamentally reshape magnonic band topology while generating unique transport signatures, thereby enabling experimental discrimination of magnonic topological phases through tunable Berry curvatures modulation. As shown in Fig. 4(a), the Berry curvatures undergo significant reconstruction around the K and K' valleys under increasing tensile strain. This reconstruction plays a key role in governing magnon transport phenomena. For example, the MHE for pristine $CrVI_6$ monolayer with SOTMI phase is approximately 5×10^{-13} W/K at 50 K as illustrated in Fig. 4(b). Although the system is in the SOTMI phase with C=0, a finite thermal Hall conductivity can still arise from the bulk magnon bands. In particular, the asymmetric distribution of Berry curvature in momentum space, together with the energy-dependent weighting function $c_2(n_B(\varepsilon))$, leads to an incomplete cancellation of contributions from different regions of the Brillouin zone, resulting in a nonzero κ^{xy} [57,58]. At the transition to TMI phase under tensile strain, the MHE increases to 2.5×10^{-12} W/K, driven by the sign reversal of the Berry curvature around the K valley. In addition, the magnon Nernst effect (MNE) [59,60], which generates a transverse spin current from a longitudinal thermal gradient, also exhibits a marked enhancement. It is given by

$$\sigma^{xy} = -\frac{k_B}{(2\pi)^2}\sum_n \int_{BZ} c_1(n_B(\varepsilon))\Omega_n^{xy}(k)\mathrm{d}k, \tag{4}$$

with $c_1(x) = (1+x)\ln(1+x) - x\ln x$. As displayed in Fig. 4(c), accompanying the TPT from SOTMI to TMI, the MNE reaches as much as $4.6\times10^{-2}\,k_B/2\pi$ from $1.6\times10^{-2}\,k_B/2\pi$. Notably, both the obtained MHE and MNE for the $CrVI_6$ monolayer are significantly exceeding the corresponding values for the CrI_3 monolayer (approximately 5×10^{-13} W/K and $6\times10^{-3}\,k_B/2\pi$) (see the SM).

Additionally, figure 4(a) indicates that Berry curvatures of the $CrVI_6$ monolayer are predominantly localized at the valley centers K and K' points, and the TPTs drive a sign reversal for Berry curvatures between the SOTMI and NMI phases. Consequently, a pronounced switch in magnonic valley transport direction emerges. To illustrate this, the valley thermal Hall conductivity κ_v^{xy} of the $CrVI_6$ monolayer under different strains are calculated with the results illustrated in Fig. 4(d). Indeed, one can clearly see that the κ_v^{xy} for SOTMI and NMI phases carry opposite signs, i.e., the valley-resolved MVHE responses provide a robust method for distinguishing the SOTMI and NMI phases. As expected, the magnon valley Nernst effect responses enables another detection and discrimination of these magnonic topological phases (see the SM).

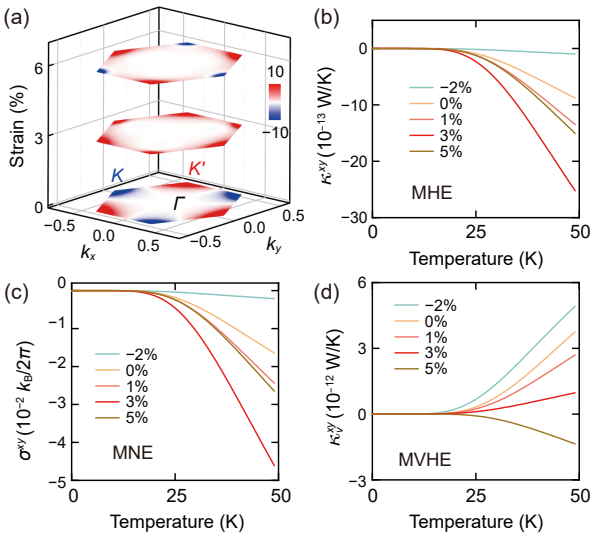

Fig. 4. (a) K-space distributions of Berry curvatures of the $CrVI_6$ monolayer under different tensile/compressive strains. Temperature dependence of (b) thermal Hall conductivity, (c) magnon Nernst conductivity, and (d) valley thermal Hall conductivity of the $CrVI_6$ monolayer under different tensile/compressive strains.

We have proposed a tunable noncentrosymmetric Heisenberg-DM platform that realizes successive topological phase transitions among the SOTMI, TMI, and NMI phases, driven by next-nearest-neighbor exchange and DM interactions. First-principles calculations identified the $CrVI_6$ monolayer as a feasible candidate, hosting an SOTMI state in equilibrium and undergoing strain-induced transitions to TMI and NMI. Notably, we identified exotic magnon transports with topological switch. The giant MHE and MNE were obtained in the $CrVI_6$ monolayer with TMI phase, while the valley-resolved MVHE

responses emerged for the SOTMI and NMI phases. Our results offer a unified theoretical and material framework for realizing and identifying tunable topological magnons in valley-polarized systems.

Acknowledgements

This work was supported by the National Natural Science Foundation of China (Grant No. 12174220), the Shandong Provincial Science Foundation for Excellent Young Scholars (Grant No. ZR2023YQ001), and the Taishan Scholar Program of Shandong Province (Grant No. tsqn202312010).

References

[1] Zhuo F, Kang J, Manchon A, and Cheng Z 2025 *Adv. Phys. Res.* **4** 2300054
[2] McClarty P A 2022 *Annu. Rev. Condens. Matter Phys.* **13** 171
[3] Hess C, Büchner B, Ammerahl U, Colonescu L, Heidrich-Meisner F, Brenig W, and Revcolevschi A 2003 *Phys. Rev. Lett.* **90** 197002
[4] Neusser S and Grundler D 2009 *Adv. Mater.* **21** 2927
[5] Lenk B, Ulrichs H, Garbs F, and Münzenberg M 2011 *Phys. Rep.* **507** 107
[6] Matsumoto R and Murakami S 2011 *Phys. Rev. Lett.* **106** 197202
[7] Chumak A V, Serga A A, and Hillebrands B 2014 *Nat. Commun.* **5** 4700
[8] Chumak A V, Vasyuchka V I, Serga A A, and Hillebrands B 2015 *Nat. Phys.* **11** 453
[9] Cornelissen L, Liu J, Duine R, Youssef J B, and Van Wees B 2015 *Nat. Phys.* **11** 1022
[10] Xing W, Qiu L, Wang X, Yao Y, Ma Y, Cai R, Jia S, Xie X, and Han W 2019 *Phys. Rev. X* **9** 011026
[11] Zhou H, Huang C, Wei N, Taniguchi T, Watanabe K, Zaletel M P, Papić Z, MacDonald A H, and Young A F 2022 *Phys. Rev. X* **12** 021060
[12] Onose Y, Ideue T, Katsura H, Shiomi Y, Nagaosa N, and Tokura Y 2010 *Science* **329** 297
[13] Bai Y, Yuan B, Chen Z, Dai Y, Huang B, Wang X, and Niu C 2026 *Phys. Rev. Lett.* **136** 046602
[14] JW G, RA G, AM L *et al*. 2026 *Chin. Phys. Lett.* **43** 020705
[15] Guo X, Zhang M H, and Yao D X 2025 *Chin. Phys. Lett.* **42** 120703
[16] Wu K, Dong J, Zhu M, Zheng F, and Zhang J 2025 *Chin. Phys. Lett.* **42** 070702
[17] Zhang L, Ren J, Wang J S, and Li B 2013 *Phys. Rev. B* **87** 144101
[18] Hirosawa T, Diaz S A, Klinovaja J, and Loss D 2020 *Phys. Rev. Lett.* **125** 207204
[19] Mook A, Henk J, and Mertig I 2016 *Phys. Rev. Lett.* **117** 157204
[20] Li Y M, Wu Y J, Luo X W, Huang Y, and Chang K 2022 *Phys. Rev. B* **106** 054403
[21] Chisnell R, Helton J, Freedman D, Singh D, Bewley R, Nocera D, and Lee Y 2015 *Phys. Rev. Lett.* **115** 147201
[22] Cai Z, Bao S, Gu Z L *et al*. 2021 *Phys. Rev. B* **104** L020402
[23] Bai Y, Zhang L, Mao N, Li R, Chen Z, Dai Y, Huang B, and Niu C 2024 *ACS Nano* **18** 13377
[24] Bai Y, Zou X, Chen Z, Li R, Yuan B, Dai Y, Huang B, and Niu C 2025 *ACS Nano* **19** 9265
[25] Chen X, Liu Y, Liu P, Yu Y, Ren J, Li J, Zhang A, and Liu Q 2025 *Nature* **640** 349
[26] Chen L, Chung J H, Gao B, Chen T, Stone M B, Kolesnikov A I, Huang Q, and Dai P 2018 *Phys. Rev. X* **8** 041028
[27] Zhu F, Zhang L, Wang X *et al*. 2021 *Sci. Adv.* **7** eabi7532
[28] dos Santos Dias M, Biniskos N, Dos Santos F, Schmalzl K, Persson J, Bourdarot F, Marzari N, Blügel S, Brückel T, and Lounis S 2023 *Nat. Commun.* **14** 7321
[29] Kasahara Y, Ohnishi T, Mizukami Y *et al*. 2018 *Nature* **559** 227
[30] Czajka P, Gao T, Hirschberger M, Lampen-Kelley P, Banerjee A, Quirk N, Mandrus D G, Nagler S E, and Ong N P 2023 *Nat. Mater.* **22** 36
[31] Bernevig B A, Hughes T L, and Zhang S C 2006 *Science* **314** 1757
[32] Xu S Y, Xia Y, Wray L *et al*. 2011 *Science* **332** 560
[33] Xu S Y, Liu C, Alidoust N *et al*. 2012 *Nat. Commun.* **3** 1192
[34] Verbin M, Zilberberg O, Kraus Y E, Lahini Y, and Silberberg Y 2013 *Phys. Rev. Lett.* **110** 076403
[35] Wang Y and Fu L 2017 *Phys. Rev. Lett.* **119** 187003
[36] Kort-Kamp W J M 2017 *Phys. Rev. Lett.* **119** 147401
[37] Longhi S 2019 *Phys. Rev. Lett.* **122** 237601
[38] Chen C, Song Z, Zhao J Z, Chen Z, Yu Z M, Sheng X L, and Yang S A 2020 *Phys. Rev. Lett.* **125** 056402
[39] Sone K, Ezawa M, Ashida Y, Yoshioka N, and Sagawa T 2024 *Nat. Phys.* **20** 1164
[40] Liu J, Zhou Y, Yepez Rodriguez S Y *et al*. 2024 *Nat. Commun.* **15** 332
[41] Peng B, Lange G F, Bennett D, Wang K, Slager R J, and Monserrat B 2024 *Phys. Rev. Lett.* **132** 116601
[42] Konig M, Wiedmann S, Brune C, Roth A, Buhmann H, Molenkamp L W, Qi X L, and Zhang S C 2007 *Science* **318** 766
[43] Uemura T, Moritake Y, Yoda T, Chiba H, Tanaka Y, Ono M, Kuramochi E, and Notomi M 2024 *Sci. Adv.* **10** eadp7779
[44] Lu Y S, Li J L, and Wu C T 2021 *Phys. Rev. Lett.* **127** 217202
[45] Holstein T and Primakoff H 1940 *Phys. Rev.* **58** 1098
[46] Bogoliubov N 1947 *J. Phys.* **11** 23
[47] Benalcazar W A, Li T, and Hughes T L 2019 *Phys. Rev. B* **99** 245151
[48] Xiao D, Yao Y, Fang Z, and Niu Q 2006 *Phys. Rev. Lett.* **97** 026603
[49] Xiao D, Chang M C, and Niu Q 2010 *Rev. Mod. Phys.* **82** 1959
[50] Hidalgo-Sacoto R, Gonzalez R, Vogel E, Allende S, Mella J D, Cardenas C, Troncoso R E, and Munoz F 2020 *Phys. Rev. B* **101** 205425
[51] Ni J, Zhang Z, Lu J, Du Q, Jiang Z, and Bellaiche L 2025 *Nano Lett.* **25** 1207
[52] Li X, Liu C, Zhang Y *et al*. 2024 *Nat. Phys.* **20** 1145
[53] He X, Helbig N, Verstraete M J, and Bousquet E 2021 *Comput. Phys. Commun.* **264** 107938
[54] Zhang H, Man X, Zhang Y, Yang W, Cui P, Xu X, and Zhang Z2024 *Phys. Rev. B* **110** 214424
[55] Moriya T 1960 *Phys. Rev. Lett.* **4** 228
[56] Soenen M, Bacaksiz C, Menezes R M, and Milošević M V 2023 *Phys. Rev. Mater.* **7** 024421
[57] Murakami S and Okamoto A 2017 *J. Phys. Soc. Jpn.* **86** 011010
[58] Moulsdale C, Pantaleón P A, Carrillo-Bastos R, and Xian Y 2019 *Phys. Rev. B* **99** 214424
[59] Cheng R, Okamoto S, and Xiao D 2016 *Phys. Rev. Lett.* **117** 217202
[60] Zyuzin V A and Kovalev A A 2016 *Phys. Rev. Lett.* **117** 217203